# Influence of the High-Temperature Mechanical Loading Mode on the Flow Behavior and Microstructural Evolution of a Nb-Stabilized Austenitic Stainless Steel

N. CLICHE, S. RINGEVAL, E. GEORGES, J. BELLUS, P. PETIT, F. CORTIAL, J.-L. HEUZÉ, and A.-F. GOURGUES-LORENZON (ORCID)

The present work addresses the effect of three high-temperature deformation modes, namely, torsion, uniaxial compression, and plane strain compression, on flow stress vs. strain curves, as well as on post-dynamic and static recrystallization of 316Nb austenitic stainless steel. Using a Hosford criterion instead of the classical von Mises criterion enables a unified description of the stress–strain curves obtained under different loading modes. This work also revealed that the loading mode had no significant effect on post-dynamic and static recrystallization phenomena. The amount of niobium atoms in solid solution might be preponderant in the control of recrystallization of 316Nb.

## I. INTRODUCTION

THE need of control of recrystallization is more and more important in the forging industry in order to optimize mechanical properties of structural components. Classical open-die forging mainly relies on compression-dominated deformation modes. On the other hand, laboratory tests used to characterize recrystallization during (or after) hot deformation use a variety of mechanical loading modes such as torsion, uniaxial compression, and plane strain compression. Transferring current knowledge from laboratory tests to industrial applications may thus involve a major change in loading mode. It is therefore of utmost importance to understand how the loading mode both impacts the values of flow stress *and* the recrystallization kinetics of metal alloys, which is still an open question in the case of hot deformation of austenitic stainless steels.

### A. *Current Knowledge About the Relationships Between the High-Temperature Loading Mode and the Flow Stress*

In order to compare flow stress vs. strain curves determined under different deformation modes, scalar equivalent stresses and strains are needed. The way these equivalent stresses and strains are calculated can influence the results of the comparison. Many authors used von Mises equivalents but the von Mises yield criterion is only a particular case, even for isotropic materials.

Many authors reported that uniaxial compression tests led to higher flow stress values than torsion tests, for a given value of equivalent strain. Namely, Gavard[1] compared hot torsion and hot compression stress–strain curves of a high-purity 304L-type austenitic stainless steel. He showed that at given von Mises equivalent strain, the von Mises flow stress was higher in compression than in torsion. Weiss *et al.*[2] compared torsion, compression, and tension flow curves for several materials using von Mises equivalent stresses and strains. They showed that the flow stress was always lower under torsion loading than under compressive and tensile loading. They also showed that equivalent strain levels corresponding to peak stresses and to the steady-state stress plateaus were lower under tension and under compression than under torsion. Thomas[3] compared hot torsion and hot compression von Mises-based flow

N. CLICHÉ is with the MINES ParisTech, PSL University, Centre des Matériaux, UMR CNRS 7633, 91003 Evry Cedex, France, Centre de Valduc, Commissariat à l'Energie atomique et aux énergies alternatives, 21120 Is-sur-Tille, France, Direction générale de l'Armement, Ministère des Armées, 60 Boulevard du Général Martial Valin, CS21623F, 75509 PARIS Cedex 15, France, and also with the CEA, Le Ponant D, 25, rue Leblanc, 75015 Paris, France. S. RINGEVAL is with the Centre de Valduc, Commissariat áEnergie atomique et aux énergies alternatives. E. GEORGES, J. BELLUS, and P. PETIT are with Aubert & Duval, BP1, 63770 Les Ancizes-Comps, France. F. CORTIAL is with Naval Group Research, Technocampus Ocean, 5 rue de l'Halbrane, 44340 Bouguenais, France. J.-L. HEUZE is with the Direction générale de l'Armement, Ministère des Armées, 60 Boulevard du Général Martial Valin, CS21623F, 75509 PARIS Cedex 15, France. A.-F. GOURGUES-LORENZON is with MINES ParisTech, PSL University, Centre des Matériaux, UMR CNRS 7633. Contact e-mail: anne-francoise.gourgues@mines-paristech.fr

curves of nickel base alloy 718. He showed that the flow stress was higher under compression by 8 to 10 pct. than under torsion. He attributed this difference to a change in the Taylor coefficient due to texture evolution during the tests. However, for low amounts of strain, no deformation-induced texture is expected to significantly develop. Tome et al.[4] deformed oxygen-free high conductivity (OFHC) copper under tension, compression, and torsion at room temperature up to a von Mises equivalent strain close to 1. They reported significant differences in flow stress between torsion and tension curves, when plotted using von Mises equivalent stresses and strains. They considered significant contributions from differences in work hardening, from departure of the experimental yield criterion from the ideal von Mises criterion, and from texture development. Zhou et al.[5] applied a mean field viscoplastic self-consistent deformation and recrystallization model on pure copper. They investigated the influence of the loading mode (namely torsion, tension, and shear) on the flow stress curve and on the dynamic recrystallization behavior. They showed that the flow stress associated with shear (representing torsion) was lower than that associated with compression.

In summary, to the authors' knowledge, the influence of the stress (and strain) equivalent used in processing of hot deformation test data into flow curves has not been rationalized yet. This is the first aim of the present work.

### B. Relationships Between the Loading Mode and the Phenomenology of Recrystallization

Humphreys et al.[6] reviewed the influence of the mechanical loading on the recrystallization phenomenon; only little knowledge was available then and no simple tendency has been reported until now in open literature. In particular, the effect of the mechanical loading mode on post-dynamic recrystallization (PDRX) was not explicitly found in the literature. Therefore, only dynamic recrystallization (DRX) and static recrystallization (SRX) are reviewed here, focusing on metals and alloys possessing a face-centered cubic (fcc) crystal structure.

Mandal et al.[7] compared the effect of high-temperature uniaxial compression vs. plane strain compression on the DRX behavior of a titanium-bearing austenitic stainless steel. The loading mode had no influence on the nucleation mechanism of DRX; yet, the kinetics of DRX was faster under uniaxial compression than under plane strain compression. These results were interpreted by considering contributions of differences in dislocation densities and in grain boundary mobility between the two deformation modes, yet, without clear experimental evidence. From Athreya et al.[8] the DRX kinetics of pure nickel was enhanced under plane strain compression with respect to uniaxial compression. Using their above-mentioned model, Zhou et al.[5] showed that dynamic recrystallization occurred at slightly lower strains after torsion than after compression. From their curves, the difference was lower than 0.02 in strain levels (for a considered strain range up to 1) and lower than 0.05 in recrystallized fractions. They

attributed this phenomenon to texture evolution but the random nucleation of new grains with dynamic recrystallization, as implemented in their model, tended to cancel the effect of texture.

Concerning SRX, Lindh et al.[9] deformed OFHC copper at room temperature either under uniaxial tension or using uniaxial compression followed by uniaxial tension. They then monitored the SRX behavior using differential scanning calorimetry with a heating rate of 10 °C.s$^{-1}$. They showed that an additive strain model clearly underestimated the recrystallization kinetics in the case of compression + tension loading, when compared to the purely tensile strain path. Embury et al.[10] used pure aluminum cubes deformed at room temperature in uniaxial compression, either monotonically or by rotating the compression direction by 90 deg after every strain increment of 0.05. They measured recrystallized fractions as a function of annealing time at 275 °C. Monotonically deformed specimens statically recrystallized earlier than those deformed in a multi-axial way to the same amount of equivalent strain. In fact, the degree or recovery of the latter was higher than that of monotonically deformed specimens. However, the kinetics of SRX was the same for both types of specimens when compared at the same level of flow stress. Barto and Ebert[11] cold deformed molybdenum up to an equivalent strain ε = 0.3. They found that the kinetics of SRX was fastest after tension, slower after drawing, even slower after rolling, and slowest after compression. They attributed this phenomenon to differences in dislocation densities produced by various deformation modes but they did not provide experimental evidence. Athreya et al.[12] compared the effect of cold torsion and cold rolling on SRX of nickel. They indicated that specimens deformed under torsion recrystallized faster than cold rolled ones. They attributed the difference to a different spatial distribution of the nuclei and of the stored energy. As a whole, there is still a lack in literature about coupling different hot deformation loading modes and measurements of recrystallization kinetics. This is the second aim of the present work.

The recrystallization behavior of 316Nb austenitic stainless steel has already been reported under torsion loading.[13,14] It has been shown that for low to moderate amounts of von Mises equivalent strain (ε ≤ 0.8), 316Nb shows a very low volume fraction of dynamically recrystallized grains. Therefore, the main recrystallization phenomena after applying such amounts of strain to this material are PDRX and SRX. For a given thermal cycle applied after hot deformation, PDRX and SRX are of course controlled by strain, strain rate, and deformation temperature but also by the initial microstructure and, in particular, by the amount of niobium atoms in solid solution. However, no estimation of the effect of hot deformation mode on the PDRX or SRX has been reported yet for this alloy family. This is the third aim of the present study.

The present work addressed the effect of the high-temperature mechanical loading mode on both the flow curves and the recrystallization behavior of austenitic 316Nb steel. To this aim, the three types of loading

modes that have been extensively used in literature were experimentally investigated, namely, torsion, uniaxial compression, and plane strain compression (channel-die), see *e.g.*, Reference 15. Mechanical analysis of experiments was carried out using both analytical methods and finite element simulations. Several equivalent criteria relevant to isotropic materials, namely, the von Mises, Tresca, and Hosford criteria were used to plot the equivalent flow stress *vs.* equivalent strain curves. Special attention was then paid to estimating *local* strains in the tested specimens. Deformed specimens underwent a slow cooling thermal cycle in order to investigate their PDRX behavior. Some of them underwent an additional isothermal annealing in order to characterize their SRX behavior. Recrystallized fractions were determined using electron backscatter diffraction (EBSD) as a function of *local* strains for the three different loading modes.

## II. EXPERIMENTAL METHODS

### A. Materials

The studied 316Nb steel was cut from a forged billet. Its chemical composition is given in Table I. All specimens of this study were machined from blanks taken from the same slice of the billet. Minimum segregation was suspected because the billet was fabricated from an electro-slag remelted (ESR) ingot and because the blanks were taken near the mid-depth of the billet.

In addition to the austenitic matrix, the steel contained a very small amount of residual $\delta$ ferrite (< 0.25 vol pct). It also contained two populations of Nb(C,N) carbonitrides, namely, coarse primary Nb(C,N) that formed close to the end of the solidification process and fine secondary Nb(C,N) that could readily precipitate and dissolve during subsequent heat treatments.

Before being machined into specimens, the blanks were heat treated in two ways (Figure 1) that led to strongly different recrystallization behaviors upon hot torsion[13,14]:

— a holding at 1100 °C during 1 hour followed by an air quench leading to a medium grain size of 130 $\mu$m and a low amount of Nb, C, and N atoms in solid solution,

— a holding at 1200 °C during 1 hour followed by an air quench leading to a larger grain size of 250 $\mu$m and a higher amount of Nb, C, and N atoms in solid solution.

These two treatments, respectively, denoted 1100 °C/1 hour and 1200 °C/1 hour hereafter, yielded a fully recrystallized microstructure. No pronounced crystallographic texture was found by X-ray diffraction.

### B. Mechanical Testing

Three types of specimens were used to apply the three considered different deformation modes as shown in Figure 2: solid torsion bars, uniaxial compression cylinders, and plane strain compression bricks (also called channel-die compression specimens, where a direction perpendicular to the compression axis, here, *y*, is blocked).

Cylindrical torsion specimens with a gage length of $L = 22$ mm and a gage radius of $R = 3$ mm were tested on a computerized hot torsion machine. They were deformed up to $\varepsilon = 0.2$ to $\varepsilon = 0.8$ von Mises equivalent strain, at a von Mises equivalent strain rate of $\dot{\varepsilon} = 0.05$ s$^{-1}$ at their outer surface and at various temperatures from 950 °C to 1150 °C. These values of temperature, applied strain, and strain rate were chosen to obtain non-recrystallized microstructures, or partially or fully recrystallized specimens after either PDRX or SRX, as reported in Reference 13. For each test, the specimen temperature was controlled using a thermocouple inserted in one specimen end; another thermocouple was attached to the gage section of the specimen. The measured difference between the bulk and the surface temperatures of the specimens was below 5 °C. The applied thermal–mechanical cycle is represented in Figure 1. For deformation temperatures lower than 1100 °C, the torsion specimens were reheated at 3 °C.s$^{-1}$ up to 1050 °C then at 0.15 °C.s$^{-1}$ up to 1100 °C. The second heating rate was lower than the first one in order to avoid any temperature overshoot. The specimens were then held at 1100 °C for 600 seconds in order to dissolve any secondary niobium-rich precipitates that could remain in the starting microstructure, while avoiding significant grain growth. This was the solutionizing step in Figure 1. Then, all specimens were brought to the deformation temperature and held for 60 seconds for temperature homogenization before being deformed. Right after deformation, they were slowly cooled down to investigate PDRX phenomena that could occur in thick-walled components (cooling rate close to 0.1 °C.s$^{-1}$ down to 600 °C and final air cooling, see Figure 1). A further annealing treatment at a unique temperature (higher than 1050 °C but lower than 1100 °C) for 2 hours with a slow heating rate (0.011 °C.s$^{-1}$) was then applied to one half of every torsion specimen, in order to investigate SRX phenomena (Figure 1). This annealing treatment ensured dissolution of embrittling Cr-rich sigma phase particles that may form during cooling after hot working of heavy components. Both hot torsion and annealing cycles were conducted under argon atmosphere to minimize specimen oxidation.

Table I.    Nominal Chemical Composition (Wt Pct) of the Considered 316Nb Stainless Steel

| Fe | Cr | Ni | Mo | Mn | Nb | Si | C | N |
|---|---|---|---|---|---|---|---|---|
| Bal. | 18 to 20 | 12 to 13 | 2.5 to 2.7 | < 2 | 0.5 to 1.0 | 0.3 to 0.5 | < 0.1 | < 0.06 |
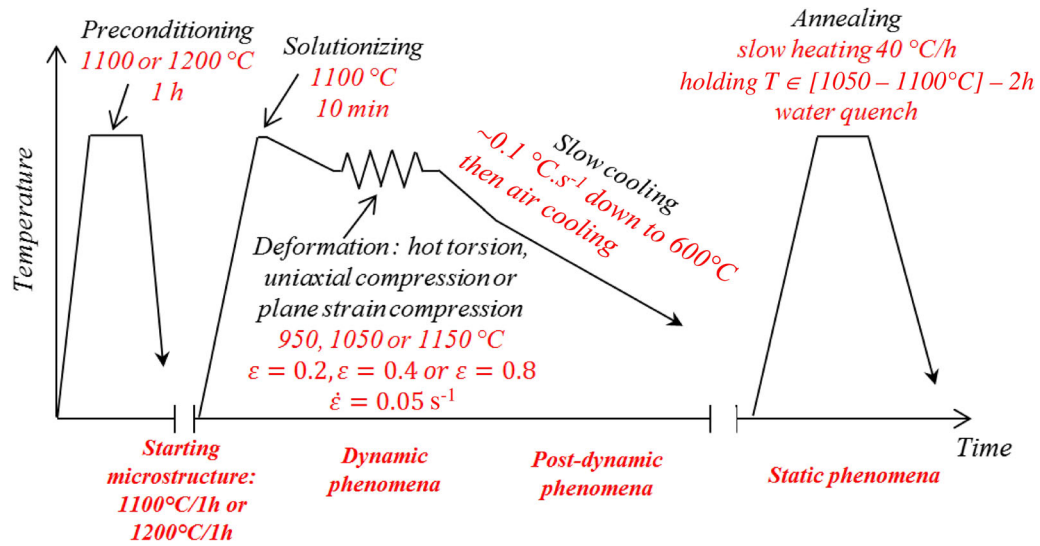
Fig. 1—Thermal cycle used for high-temperature deformation tests.



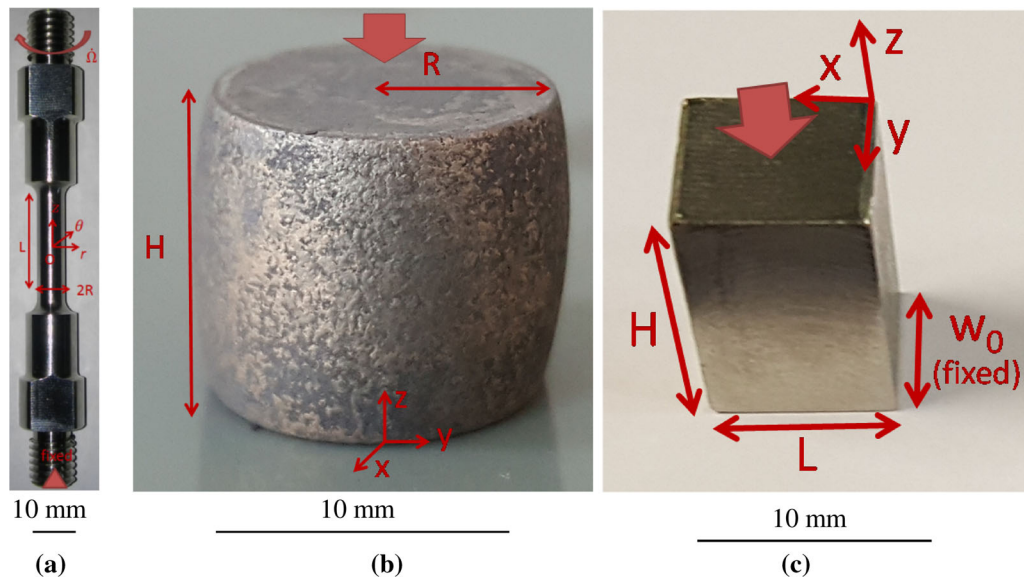| 10 mm | 10 mm | 10 mm |
| :---: | :---: | :---: |
| **(a)** | **(b)** | **(c)** |

Fig. 2—Schemes of the three types of deformation modes considered, superimposed on photographs of the corresponding specimens; (*a*) torsion (before testing), (*b*) uniaxial compression (after testing), (*c*) plane strain compression (before testing). For torsion specimens, the origin of the (*x,y,z*) frame is at the center of the gage part. For compression specimens, the origin is at the center of the bottom face.

Uniaxial compression cylinders of radius $R_0 = 6$ mm and height $H_0 = 18$ mm were used (Figure 2(b)). These dimensions provided a good combination between minimization of friction and of the risk of buckling. Graphite and boron nitride layers were deposited on the specimens to ensure good lubrication at high temperature. The specimens were deformed in a servohydraulic machine between two titanium–zirconium–molybdenum alloy (TZM) anvils to nominal von Mises deformation of $\varepsilon = 0.2$ or $\varepsilon = 0.4$ at constant nominal von Mises strain rate of $\dot{\varepsilon} = 0.05$ s$^{-1}$ and at temperatures ranging from 950 °C to 1150 °C. The temperature was measured by a thermocouple attached to the anvils. Displacements were measured by a linear variable differential transformer (LVDT) sensor and forces were measured by a

load cell. The same thermal cycles (Figure 1) were applied except for the heating rate, which was limited to 1.67 °C.s$^{-1}$ instead of 3 °C.s$^{-1}$ (this was supposed to have no influence on the results). Due to the small size of these specimens, final annealing was done on entire specimens and not on specimen halves to avoid decarburization-induced artifacts that can occur close to the specimen surface at high temperature. Therefore, only a few specimens were analyzed after only slow cooling and most specimens were analyzed after having experienced both slow cooling and annealing. Both compression and annealing cycles were conducted under argon atmosphere.

Plane strain compression specimens (Figure 2(c)) were parallelepipeds of height $H_0 = 12$ mm, length $L_0 = 8$

mm, and width $w_0 = 7$ mm. The same graphite and boron lubrication was used as for uniaxial compression. The specimens were deformed in the same hydraulic machine as uniaxial compression specimens; yet, the device was adapted to ensure plane compression. Two side walls constrained the specimen along the $y$ axis. A small gap remained at the beginning of the test to ensure easy closing of the device during the test. These specimens were deformed up to nominal von Mises strains of 0.2 and 0.4 at the same nominal von Mises constant strain rate of $\dot{\varepsilon} = 0.05$ s$^{-1}$ and at temperatures of 950 °C and 1050 °C. Temperature, displacement, and load measurements were performed as for uniaxial compression. The final annealing was applied to all specimens (therefore PDRX was not characterized for plane strain specimens). Both compression and annealing cycles were conducted under argon atmosphere.

### C. Quantification of Recrystallized Fractions

In the present work, non-recrystallized grains exhibited a high level of recovery, as already reported in Reference 13. Consequently, no significant difference in hardness could be evidenced between recrystallized and non-recrystallized regions.

The fraction of recrystallized grains was determined using internal crystal misorientations. To this aim, EBSD maps were acquired for all tested specimens. After conventional polishing with a colloidal silica finish, EBSD patterns were acquired using a Nova NanoSEM 450 field emission gun scanning electron microscope equipped with a Hikari EBSD camera and the EDAX OIM® EBSD software. The microscope was operated at 20 kV with a tilt angle of 70 deg. The acquisition step size was adapted to the various specimens, either 2 $\mu$m (torsion and uniaxial compression specimens) or 5 $\mu$m (larger maps from plane strain compression specimens), in order to cover a sufficient amount of grains within a reasonable amount of time. Details about the selection of the scanned regions, adapted to every type of specimen, are given in the next section. Data noise reduction was carried out using a dilation procedure. More than 95 pct of the data points were reliably indexed in most of the raw datasets; poorly indexed points were mainly located at grain boundaries. The absence of data reduction artifacts was checked by comparing *e.g.*, inverse pole figure maps of raw and processed data from a given EBSD map.

The grain orientation spread (GOS) parameter was used to quantify recrystallized fractions by considering two estimates. It was calculated in each grain by first determining the average orientation $\Omega$ of the grain, then by calculating the average misorientation between $\Omega$ and the crystal orientation at each measurement point of that grain. Grains with a GOS lower than 1 deg were considered to estimate the lower bound of the recrystallized fraction; grains with a GOS lower than 2 deg were considered to get an upper bound. Among other advantages, the GOS parameter is less sensitive to localized hardening induced by residual polishing scratches than more local criteria such as the kernel average misorientation. It is not very sensitive to the

step size; in the present coarse-grained material, using a 5-$\mu$m step size did not alter GOS measurements.

## III. MECHANICAL AND MICROSTRUCTURAL ANALYSIS METHODOLOGY

In order to precisely analyze the differences in flow stress and recrystallized fractions, a proper description of stress and strain state in the specimens was needed. It was used to process data into flow curves and also to select relevant regions for EBSD mapping. The frame and geometrical parameters of the three kinds of specimens are shown in Figure 2.

The strain rate tensors for, respectively, torsion, uniaxial compression, and plane strain compression tests are represented in the frames of Figure 2 as follows:

$$\underline{\varepsilon} = \begin{pmatrix} 0 & 0 & 0 \\ 0 & 0 & r \\ 0 & r & 0 \end{pmatrix} \frac{\dot{\Omega}}{2L} \ \text{for hot torsion} \quad [1]$$

$$\underline{\varepsilon} = \begin{pmatrix} -1/2 & 0 & 0 \\ 0 & -1/2 & 0 \\ 0 & 0 & 1 \end{pmatrix} \frac{\dot{H}}{H} \ \text{for uniaxial compression} \quad [2]$$

$$\underline{\varepsilon} = \begin{pmatrix} -1 & 0 & 0 \\ 0 & 0 & 0 \\ 0 & 0 & 1 \end{pmatrix} \frac{\dot{H}}{H} \ \text{for plane strain } (channel-die) \ compression \quad [3]$$

### A. Torsion Tests

For torsion specimens, the classical analysis makes use of the Fields and Backofen equation[16] relating the shear stress at the outer radius of the specimen $R$, $\tau(R)$ to the torque, $\Gamma$:

$$\tau(R) = \frac{\Gamma}{2\pi R^3} \left( 3 + \frac{\partial \ln \Gamma}{\partial \ln N} + \frac{\partial \ln \Gamma}{\partial \ln \dot{N}} \right) \quad [4]$$

In Eq. [4], $N$ is the number of cycles underwent by the torsion specimen.

Let us, respectively, denote $\tilde{n} = \frac{\partial \ln \Gamma}{\partial \ln N}$ and $\tilde{m} = \frac{\partial \ln \Gamma}{\partial \ln \dot{N}}$ the strain and strain rate sensitivities. The values of $\tilde{n} = 0.10$ and $\tilde{m} = 0.1426$ were determined from various stress–strain curves. Regarding the strain sensitivity, a unique value was selected over the whole strain range rather than a moving average because moving averages lead to overestimated flow stress at the beginning of the test. The strain rate sensitivity is consistent with those reported in References 13 and 17.

In the Fields and Backofen method, a von Mises criterion is then used to get the stress–strain curve:

$$\varepsilon_{eq}^{VM} = \frac{2\pi N R}{L\sqrt{3}} \quad \sigma_{eq}^{VM}(R) = \frac{\Gamma \sqrt{3}}{2\pi R^3} (3 + \tilde{n} + \tilde{m}) \quad [5]$$

Other criteria can also be considered to represent the multi-axial behavior of the material. The material considered was initially isotropic and only small amounts of strain were applied, leading to very small texture formation. Therefore, only isotropic criteria were considered. They all lay between Tresca and von Mises criteria. The Hosford criterion[18] encompasses both Tresca and von Mises criteria in a single mathematical equation. It was expected to be a very interesting way to reproduce the multi-axial behavior of 316Nb. The general expression of the yield function is recalled as follows:

$$f(\sigma) = \left( \frac{|\sigma_1 - \sigma_2|^n + |\sigma_2 - \sigma_3|^n + |\sigma_1 - \sigma_3|^n}{2} \right)^{\frac{1}{n}} \quad [6]$$

In Eq. [6], $\sigma_1$, $\sigma_2$, and $\sigma_3$ are the principal stresses and $n$ is a scalar greater than or equal to 1. For $n = 2$, one finds the von Mises yield surface and for $n$ going to infinity, one finds the Tresca yield surface.

For torsion specimens, using the Hosford criterion leads to the following expressions for the equivalent strain and stress:

$$\varepsilon_{eq}^H = \frac{2\pi N R}{L \left(1 + 2^{n-1}\right)^{\frac{1}{n}}}$$

$$\sigma_{eq}^H(R) = \frac{\Gamma \left(1 + 2^{n-1}\right)^{\frac{1}{n}}}{2\pi R^3} (3 + \tilde{n} + \tilde{m}) \quad [7]$$

The value of the Hosford exponent $n = 20$ was determined using a polycrystalline self-consistent numerical model (see Appendix A). Using this criterion, respectively, led to a 12 pct increase and a 3 pct decrease in flow stress (for given equivalent strain) compared to, respectively, von Mises and Tresca criteria (Figure A1(b) of Appendix A).

To perform EBSD measurements, the side surface of tested torsion specimens was slightly polished, over a depth of 100 to 500 micrometers. The size of the EBSD scanned zones was 0.8 mm × 2.3 mm.

Therefore, the distance to the specimen axis (the actual value of R) was adjusted to its actual range of values in the mapped region using simple trigonometry relationships. From Eq. (1), a proportionality rule was then used to estimate the strain experienced there. The ratio of the local strain to the equivalent strain at outer radius ranged between 0.92 and 0.98. This was the first (geometrical) correction factor. In addition, the use of a different expression for equivalent strains multiplied the local strain by 0.87 for a Tresca criterion, and by 0.9 for the selected Hosford 20 criterion, with respect to that estimated using the von Mises criterion. This was the second correction factor. By multiplying the two correction factors, the overall reduction in strain compared to that calculated at the outer surface using a von Mises criterion was assumed to be between 0.8 and 0.88. These correction factors were used to calculate local strains relevant to EBSD maps.

## B. Analysis of Uniaxial and Plane Strain Compression Tests Using an Analytical Model

The classical analysis of compression tests[19] assumes that the strain rate tensor is uniform and that friction is taken into account by an energy balance, namely, that a part of deformation energy is dissipated in friction work according to Tresca modeling. In the following, $\overline{m}$ is the Tresca friction coefficient. Its value was assumed to be constant during the test, and identical for the two kinds of compression tests that used identical lubrication conditions.

As already stated, the chosen equivalent criterion is of utmost importance for torsion tests. However, this is less important for compression tests. For pure uniaxial compression, the various equivalent criteria coincide. Therefore, assuming that the experimental uniaxial compression test (with some barreling as seen in Figure 2) is not very different from the purely uniaxial case, one can use von Mises formulae for strain and stress:

$$\varepsilon_{eq} = \sqrt{\frac{2}{3}\underline{\varepsilon} : \underline{\varepsilon}} = -\ln\left(\frac{H}{H_0}\right) \quad \sigma_{eq} = \frac{F}{\pi R^2} \left(1 + \frac{2}{3\sqrt{3}}\overline{m}\frac{R}{H}\right)^{-1}$$

$$[8]$$

In Eq. [8], $R$ and $H$ are, respectively, the current radius and the current height of the specimen, $H_0$ is its initial height, and F is the applied load.

For plane strain compression, the criteria differ but, by analogy, the von Mises criterion was selected, recalling the analysis of Chovet et al.[20]:

$$\varepsilon_{eq} = \frac{2}{\sqrt{3}}\ln\left(\frac{H_0}{H}\right) \quad [9]$$

$$\sigma_{eq} = \frac{F}{Lw_0} \left(1 + \frac{\overline{m}}{L_0 H_0 w_0}(w_0 \frac{L^2}{4} + \frac{L^3}{48}\ln\left(\frac{\sqrt{4H^2 + L^2} + 2H}{\sqrt{4H^2 + L^2} - 2H}\right)\right.$$
$$\left. + \frac{H^3}{6}\left(\frac{\sqrt{4H^2 + L^2} + L}{\sqrt{4H^2 + L^2} - L}\right) + \frac{HL}{6}\sqrt{4H^2 + L^2}))^{-1}$$

$$[10]$$

In Eqs. [9] and [10], $L$ and $H$ are, respectively, the current length and height of the specimen; $L_0$, $H_0$ are its initial length and height; $w_0$ is its fixed width; and $F$ is the applied load.

It is worth noting that the formula reported by Chovet et al.[20] wrongly gives a term in $\frac{w_0 L^2}{12}$ instead of $\frac{w_0 L^2}{4}$, which has been corrected here.

These formulae were used to analyze the flow stress of compression specimens. However, they assume no heterogeneity of strain in the specimens which may be a good assumption for global quantities like stress–strain curve but not for local microstructural analysis using EBSD. Therefore, FEM simulations of the compression tests were also carried out.

## C. Finite Element Analysis of Uniaxial and Plane Strain Compression Tests and Selection of Relevant Regions for Microstructural Analysis

Finite element simulation of uniaxial compression tests was done using Forge NxT2® software.[21] The nominal geometry, a Hensel–Spittel flow stress equation[22] and a Tresca friction coefficient were used. The flow stress parameters were taken from an internal database available for the considered material. The friction coefficient was set to $\overline{m} = 0.3$ in order to well reproduce the final geometry of the deformed specimens. The same parameters were used for both initial microstructures. The mesh size was 0.5 mm for uniaxial compression and 0.3 mm for plane strain compression. A nominal strain of $\varepsilon = 0.2$ at $T = 950^{\circ}$C and of $\varepsilon = 0.4$ at $T = 1050^{\circ}$C were considered in view of the above-mentioned experimental conditions. The nominal strain rate was set to $\dot{\varepsilon} = 0.05$s$^{-1}$.

Von Mises equivalent strains maps are shown in Figure 3 for uniaxial compression tests. They reproduced the experimentally observed barreling. They also showed that deformation tended to concentrate at the center of the specimen and that weakly deformed "dead zones" were present close to the anvils. For these reasons, comparing deformation modes without taking these heterogeneities into account could lead to confusion: an enhanced recrystallization in the center of a compression specimen cannot be attributed to the deformation mode solely because there is an additional contribution of geometrical effects.

In order to properly take this effect into account, EBSD patterns were acquired both at the center of specimens and at the so-called "mid-distance" between the center and the upper anvil (Figure 3). As in the case of torsion, the size of the scanned zone was 0.8 mm × 2.3 mm. Thanks to numerical simulations, the corresponding local strains were estimated, as reported in Table II.

FEM simulations of plane strain compression tests were carried out for nominal strains $\varepsilon = 0.2$ and $\varepsilon = 0.4$.

Von Mises equivalent strain maps are shown in Figure 4. An initial gap of 0.1 mm was introduced on each side. This gap was necessary in the real experiment to close the device. Simulations revealed that the gap had a strong influence on the flow stress curve: at the beginning of the test, the gap was not closed and the specimen was loaded under uniaxial compression, then the widening specimen progressively reached the channel wall so that it finally deformed in purely plane strain conditions. Channel walls were considered fixed as in the experiment. This led to a dissymmetrical final geometry, the specimen section being larger close to the top part and lower close to the bottom part. This is explained by the difference in friction between the top and the bottom parts of the specimen. This effect is readily visible on the tested specimens.

To take this heterogeneity into account, EBSD patterns were acquired over the entire specimen height at mid-width. The width of EBSD maps themselves was 0.8 mm; recrystallized fractions were extracted at the center, where the local strains were estimated (see Table II).

## IV. FLOW STRESS RESULTS

Flow stress curves were calculated using the above methodology. Torsion and uniaxial compression curves exhibited remarkable repeatability. Plane strain compression tests yielded more scattered results due to the above-mentioned contact issues; they are analyzed separately.

## A. Torsion and Uniaxial Compression

Figure 5 shows that for a given deformation condition, on the one hand, torsion flow stress curves analyzed with the von Mises criterion were significantly lower than uniaxial compression stress curves, which is consistent with References 1 and 3. On the other hand, torsion stress curves analyzed with the Tresca yield
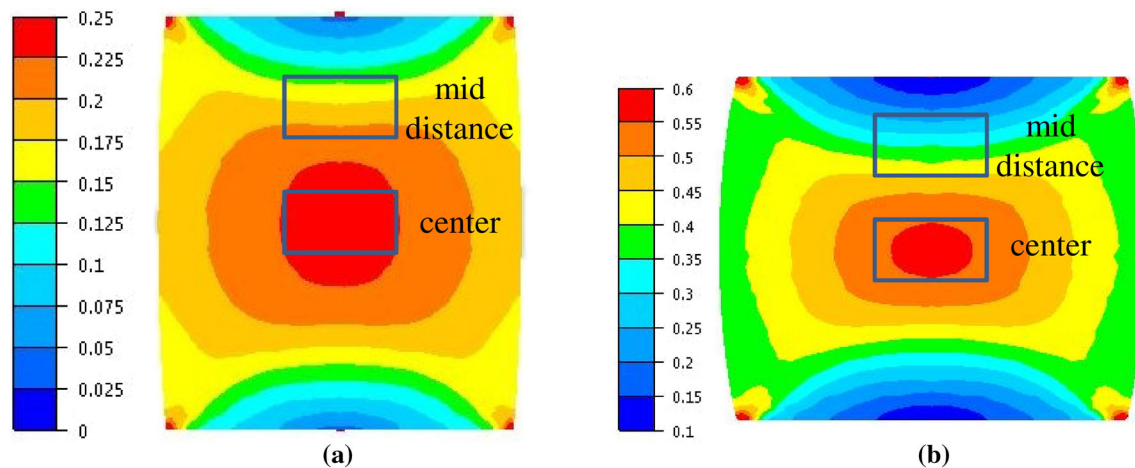


**(a)**          **(b)**

Fig. 3—Cumulative plastic strain maps obtained by FEM of uniaxial compression tests, section parallel to the compression direction, and containing the specimen axis; (a) deformed at $\varepsilon = 0.2$ and at T = 950 °C, (b) deformed at $\varepsilon = 0.4$ and at T = 1050 °C. The boxes schematize the location of regions analyzed with EBSD.

criterion were slightly above uniaxial compression stress curves. Torsion stress curves analyzed with the Hosford 20 criterion were close to those analyzed with Tresca and were remarkably close to uniaxial compression curves. For this isotropic material, using a Hosford criterion, the difference between flow curves, respectively, obtained in torsion and in uniaxial compression vanished.

## B. *Plane Strain Compression*

Plane strain compression stress–strain curves are represented in Figure 6. They clearly show the two above-mentioned two stages, namely, uniaxial compression until the specimen is in full contact with the walls, and then, plane strain compression where the flow stress increases a lot. The amount of strain at which the load strongly increased varied between $\varepsilon = 0.10$ and $\varepsilon = 0.25$ and was not very reproducible. Comparison with uniaxial compression curves indicates that the friction correction was too high in the first phase (only a uniaxial correction should be done) and too low in the second phase. Due to these effects, experimental flow stress curves of plane strain compression tests were difficult to analyze. Analytical friction corrections were not adapted in practice, due to the importance of the initial gap.

## V. MICROSTRUCTURAL RESULTS

### A. *Typical Microstructures as Revealed Using EBSD Mapping*

The evolution of grain size and shape during deformation, subsequent cooling, and final annealing is illustrated with typical examples in Figure 7. After deformation up to 0.2, no significant change in grain size and shape was noticed. After deformation up to 0.4 or more, non-recrystallized grains appeared elongated along a direction tilted with respect to the axis of torsion specimens (Figures 7(a) through (d)), and elongated perpendicular to the axis of compression specimens (Figures 7e,f). In non-recrystallized grains, annealing twins appeared heavily deformed (Figure 7a, center of Figure 7(e)), making it difficult to separate them from grain boundaries as reported in[13]. For this reason, optical micrographs were not used to investigate grain morphology. Recrystallized grains resulting either from PDRX (Figures 7(a), (b), (e), (f)) or from SRX (Figures 7(b), (c)) were much smaller, equiaxed in shape, and contained well-defined annealing twins.

Representative examples of EBSD maps are shown for torsion (Figure 8), uniaxial compression (Figure 9), and plane strain compression specimens (Figure 10). Being mainly used for quantitative recrystallized fraction assessment in Figure 11 and Figure 12, only typical examples of GOS spatial distributions are displayed here.

From the EBSD maps of Figure 10, the center was well recrystallized, regions between the center and the top (or bottom) tended to be partially recrystallized,

whereas the top and bottom parts could be little or even not recrystallized at all, depending on the testing conditions. This confirmed the need to match EBSD patterns to *local* strain estimates. By considering Figure 8 and by comparing Figures 9 and 10 with Figures 4(a) and (b), respectively, the recrystallized fraction clearly increases with the increase in amount of applied strain.

## B. *Post-dynamic Recrystallization*

Figure 11 shows the recrystallized fraction following slow cooling as a function of the estimated cumulative plastic strain. Intervals mentioned in Table II are reported as error bars along the horizontal axis. Error bars along the vertical axis are delimited by fractions of grains with GOS lower than 1 and 2 deg, respectively. As already mentioned in the Introduction section and consistently with Reference 13, no DRX was expected to occur at strains lower than 0.4; therefore, the recrystallized fraction was attributed to PDRX in the following.

Regarding the 1100 °C/1 hour specimens deformed at 1050 °C (Figure 11(a)), the recrystallized fraction increased with applied strain and no difference in the growing tendency could be seen between torsion and uniaxial compression.

Regarding the 1200 °C/1 hour specimens deformed at 950 °C (Figure 11(b)), the recrystallized fraction was almost zero in torsion as well as in uniaxial compression. Regarding the 1200 °C/1 hour specimens deformed at 1150 °C (Figure 11(c)), the recrystallized fraction globally increased with applied strain, with some scatter and rather low values near $\varepsilon = 0.4$. Nucleation could have occurred abruptly once a given strain level was reached under compression and these regions might be at the brink of starting to recrystallize. Other tests are needed to more deeply investigate the particular behavior of this region of the compression specimens.

From these results, it was concluded that in the considered 316Nb steel, PDRX was not significantly influenced by the deformation mode in the investigated ranges of initial heat treatments, strain, strain rate, and deformation temperature. This implies that PDRX, with a good approximation, could be studied and modeled regardless of the deformation mode.

## C. *Static Recrystallization*

Figure 12 shows the recrystallized fraction following slow cooling and final annealing, as a function of the estimated strain.

At 950 °C, PDRX was very limited for both initial heat treatments, at least in torsion specimens.[13] Therefore, the recrystallized fraction at this temperature was attributed to SRX.

At 1050 °C and 1150 °C, especially for 1100 °C/1 hour specimens, both PDRX and SRX were expected to occur. As shown in the previous section, PDRX was insensitive to the deformation mode. Consequently, it was considered that the effect of the deformation mode on the sole SRX part, if any, would be the main contribution to the results here.

| Nominal Strain (von Mises Equivalent) | Local Strain at the Observed Depth for Torsion Specimens | Local Strain at Center for Uniaxial Compression Specimens | Local Strain at Mid-distance Between Center and Anvil for Uniaxial Compression Specimens | Local Strain at Center for Plane Strain Compression Specimens |
|---|---|---|---|---|
| 0.2 | [0.160 to 0.176] | [0.225 to 0.250] | [0.125 to 0.200] | [0.210 to 0.250] |
| 0.4 | [0.320 to 0.352] | [0.550 to 0.600] | [0.350 to 0.400] | [0.450 to 0.600] |
| 0.8 | [0.640 to 0.704] | not used | not used | not used |
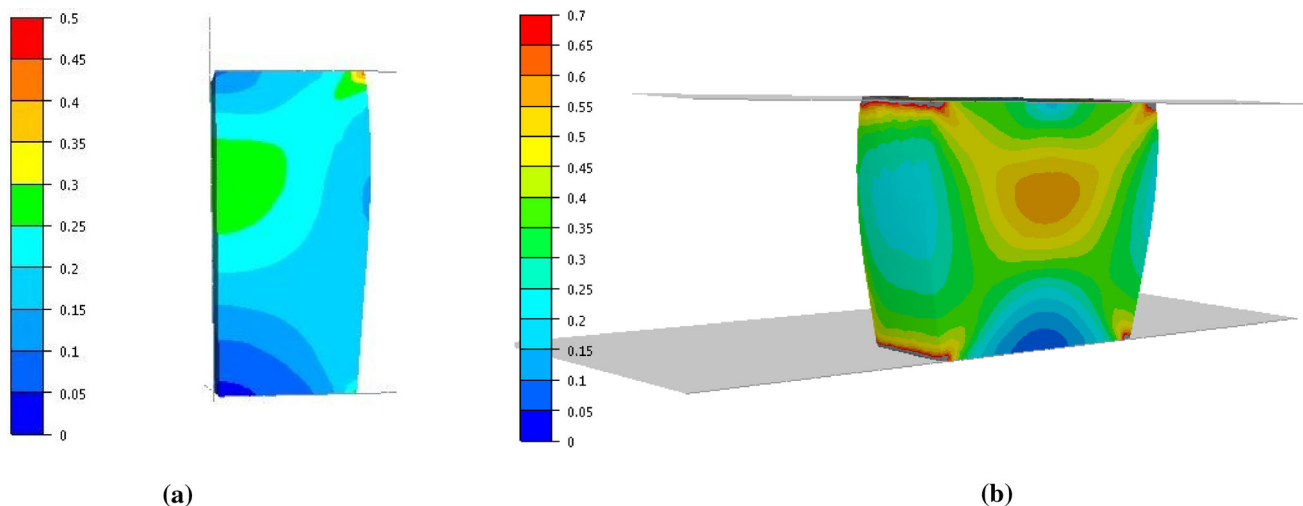


Fig. 4—Cumulative plastic strain maps obtained by FEM of plane strain compression tests at T = 1050 °C, (a) $\varepsilon$ = 0.2, (b) $\varepsilon$ = 0.4. For symmetry reasons, only one half of the specimen is represented, the large face shown here being at mid-width. The compression axis is vertical.

All 1100 °C/1 hour specimens deformed at 1150 °C, then annealed, were fully recrystallized. Therefore, no effect of the deformation mode was observed. When deformed at 1050 °C, the recrystallized fraction increased with applied strain; data from torsion, uniaxial compression, and plane strain compression specimens were very consistent with each other. There was thus no visible effect of the deformation mode on the recrystallized fraction.

For 1200 °C/1 hour specimens deformed at 950 °C or at 1150 °C, a unique tendency was visible: the recrystallized fraction increased with applied strain independently of deformation mode. When deformed at 1050 °C, results were more spread-out (especially for the uniaxial compression point near $\varepsilon$ = 0.2) but no influence of the deformation mode could be inferred. The high scatter of data for this temperature is understandable because it concentrates both uncertainties of PDRX and SRX.

From these results, it was concluded that SRX was not significantly influenced by the deformation mode in the investigated ranges of initial heat treatments, strain, strain rate, and deformation temperature. This implies that SRX, with a good approximation, could be studied and modeled regardless of the deformation mode.

## VI. DISCUSSION

In this section, we first discuss possible origins of flow stress differences observed between torsion and uniaxial compression when plotted with a von Mises criterion, and how a Hosford 20 criterion can describe both curves in a unified manner. Then, we discuss the physical reasons for which one might expect differences in recrystallization kinetics between torsion, uniaxial compression, and plane strain compression specimens, and why this is not significant in our case.

### A. About Possible Effects of the Loading Mode on Flow Stress Curves for the Different Stress and Strain Equivalents Used

The three reasons given by Tome et al.[4] to interpret differences between uniaxial compression and torsion flow stress levels, when plotted with a von Mises criterion, were recalled in the Introduction section. They are analyzed here in view of the present results.

– The contribution of "texture development" cannot explain the difference observed in this work because no initial texture was present before deformation. The main difference in strain hardening appeared for
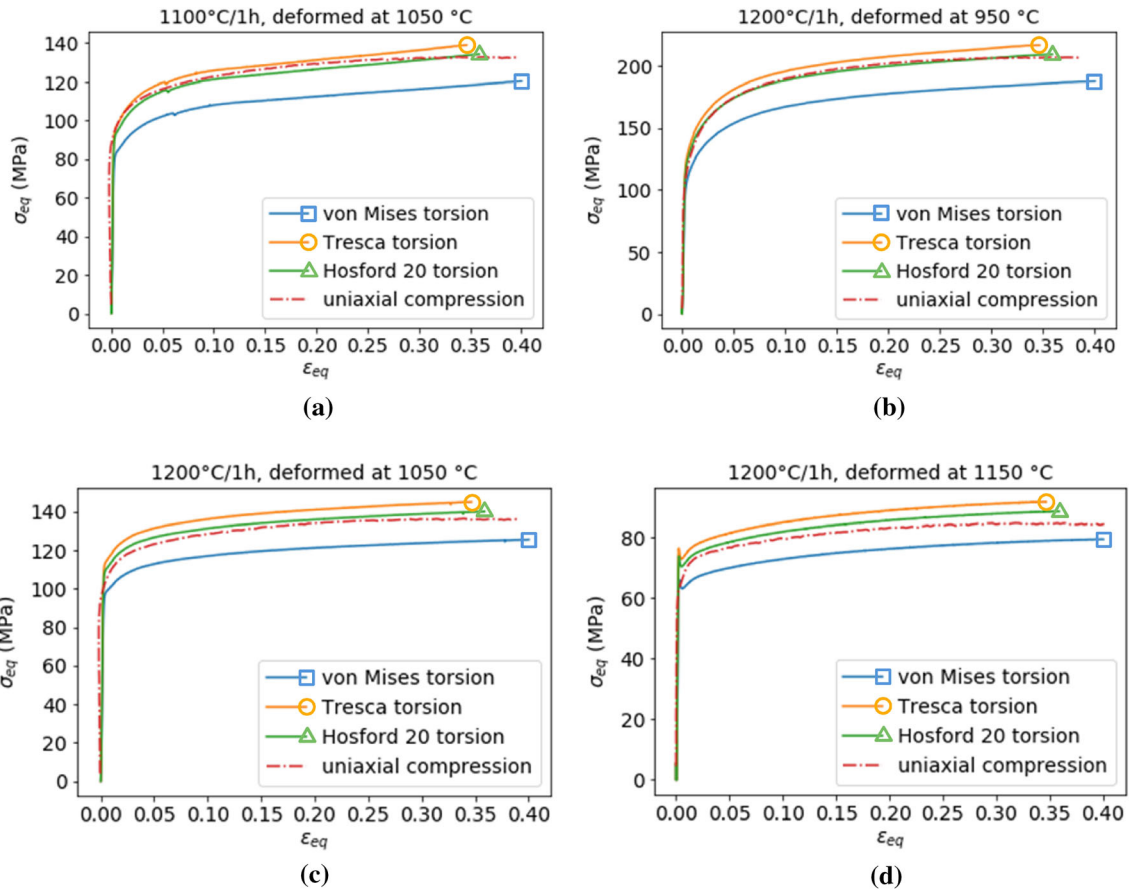
Fig. 5—Comparison between torsion and uniaxial compression flow stress curves; specimens heat treated at (*a*) 1100 °C and (*b-d*) 1200 °C, deformed at 950 °C (b), 1050 °C (a, c), and 1150 °C (d). In addition to colors, one specific symbol was added at the final point of the curves for easier reference to the testing conditions.
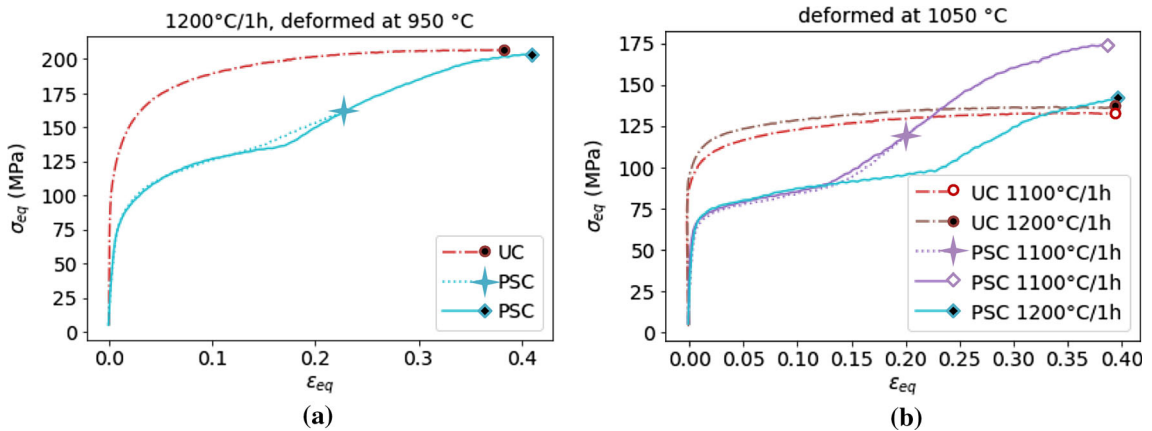


Fig. 6—Comparison between plane strain compression (PSC) and uniaxial compression (UC) flow stress vs. cumulative plastic strain curves (von Mises equivalents). (*a*) Deformation at 950 °C; (*b*) deformation at 1050 °C for two different starting microstructures. In addition to colors, one specific symbol was added at the final point of the curves for easier reference to the testing conditions.

very low amounts of strain (*i.e.*, at departure from linear behavior). Such small strain levels are too low to generate significantly different textures between uniaxial compression and torsion specimens; in fact, no significant texture could be evidenced from the analysis of EBSD maps of tested specimens.

– The "difference in work hardening rate" at low strains (less than 0.01 as seen in the beginning of the curves in Figure 5, Figure 6, or Figure A1) is the principal contribution to the differences between torsion and uniaxial compression curves when plotted with a von Mises criterion. For strain levels
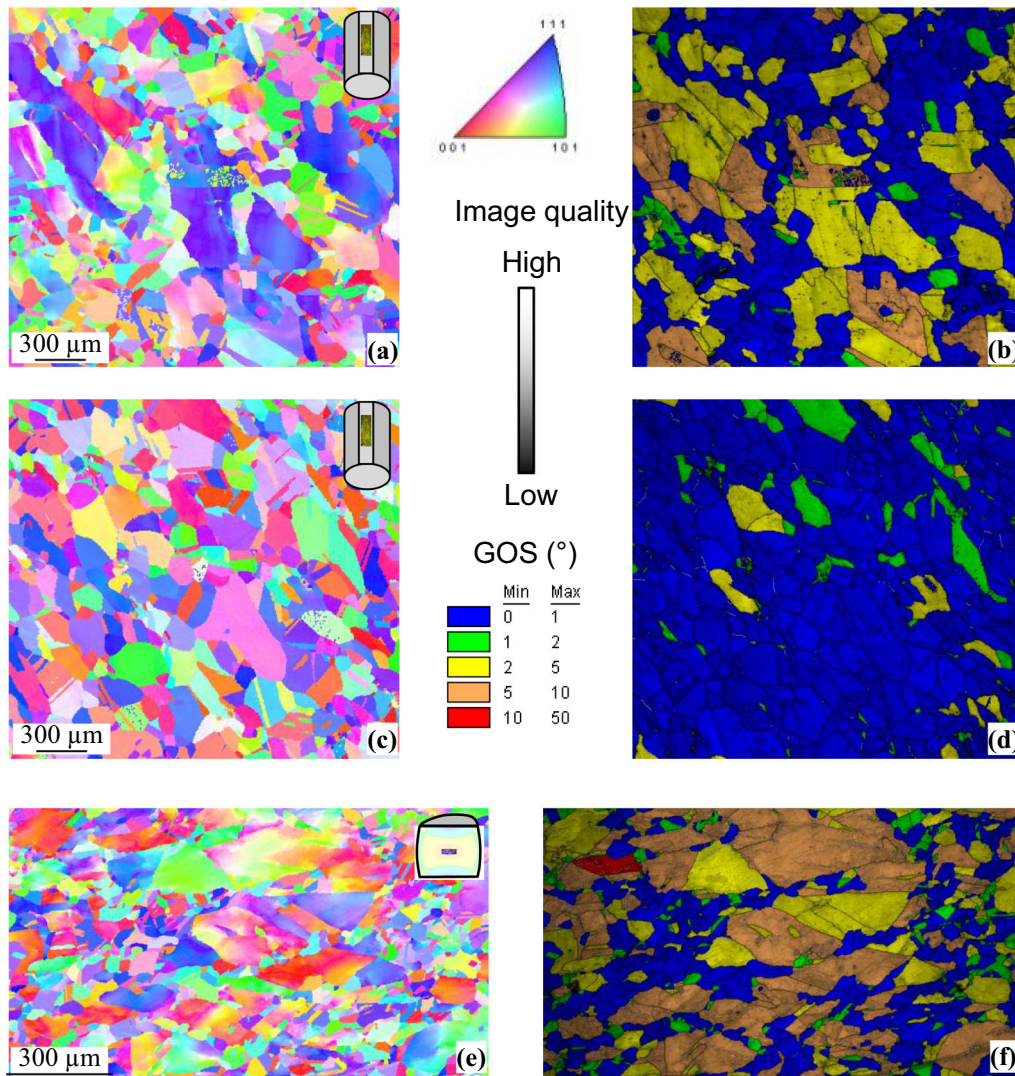
Fig. 7—(a, c) EBSD inverse pole figure maps (vertical axis), (e) EBSD inverse pole figure map (sample normal), and (b, d, f) combined image quality + GOS maps of torsion and compression specimens. (a,b) 1100 °C/1 hour torsion specimen, deformed at 1050 °C up to $\varepsilon = 0.4$ then slowly cooled (recrystallized fraction close to 0.5). (c,d) Same specimen after final annealing (recrystallized fraction close to 0.9). (e,f) Central region of the 1200 °C/1 hour compression specimen deformed at 1150 °C up to $\varepsilon = 0.4$ (recrystallized fraction close to 0.4). The location of the maps in the specimens is recalled in (a,c,e). The loading axis is vertical.

higher than about 0.02, the flow curves almost superimposed to each other by a simple translation along the (vertical) stress axis, showing similar work hardening. As the strain field in torsion specimens is not homogeneous, progressive development of incipient plasticity, governed by the yield criterion, could strongly impact the very beginning of the flow curve derived from the torsion test. Consequently, it is thought that the apparent difference in work hardening rate still might be mainly linked to the yield criterion used.

– The "departure of the actual yield criterion of the material from the von Mises criterion" is the major explanation retained here: the present work showed that using Tresca or Hosford criteria changed the flow stress comparison a lot. Using a self-consistent approach of the viscoplastic behavior of a polycrystalline aggregate (Appendix A) showed that a Hosford 20 criterion was able to superimpose torsion and uniaxial compression curves.

As a result, one may consider that the difference between compression flow stress and torsion flow stress vs. strain curves is strongly linked to the use of von Mises criterion, and that a Hosford 20 criterion gives a practical way to describe torsion and uniaxial compression flow stress curves in a unified manner. In this work, it was not possible to use plane strain compression curves to check whether the Hosford criterion was also able to address this deformation mode because of the above-mentioned friction and boundary conditions issues. The use of dedicated specimens, without contact issues, in e.g., torsion–traction experiments could clarify this point.
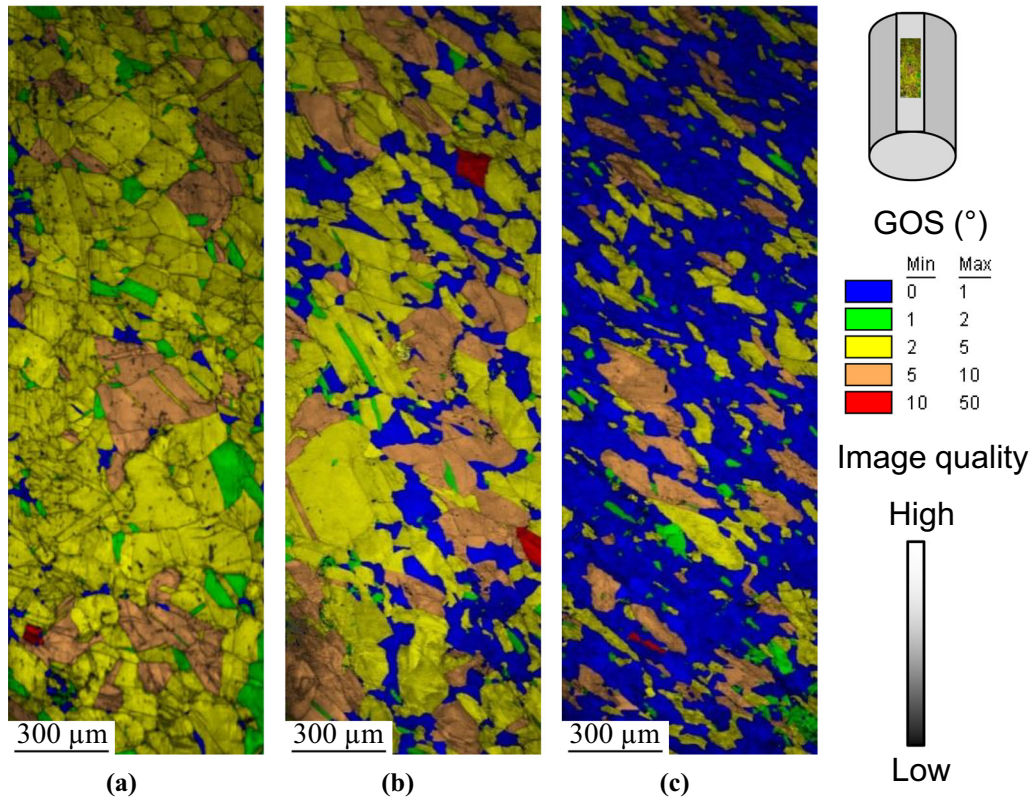
Fig. 8—EBSD maps of torsion specimens (GOS and image quality), 1200 °C/1 hour deformed at 1050 °C, after slow cooling and final annealing, (*a*) $\varepsilon = 0.2$, (*b*) $\varepsilon = 0.4$, and (*c*) $\varepsilon = 0.8$. The location of the maps, close to the outer surface of the specimens, is recalled in the top right scheme. The torsion axis is vertical.
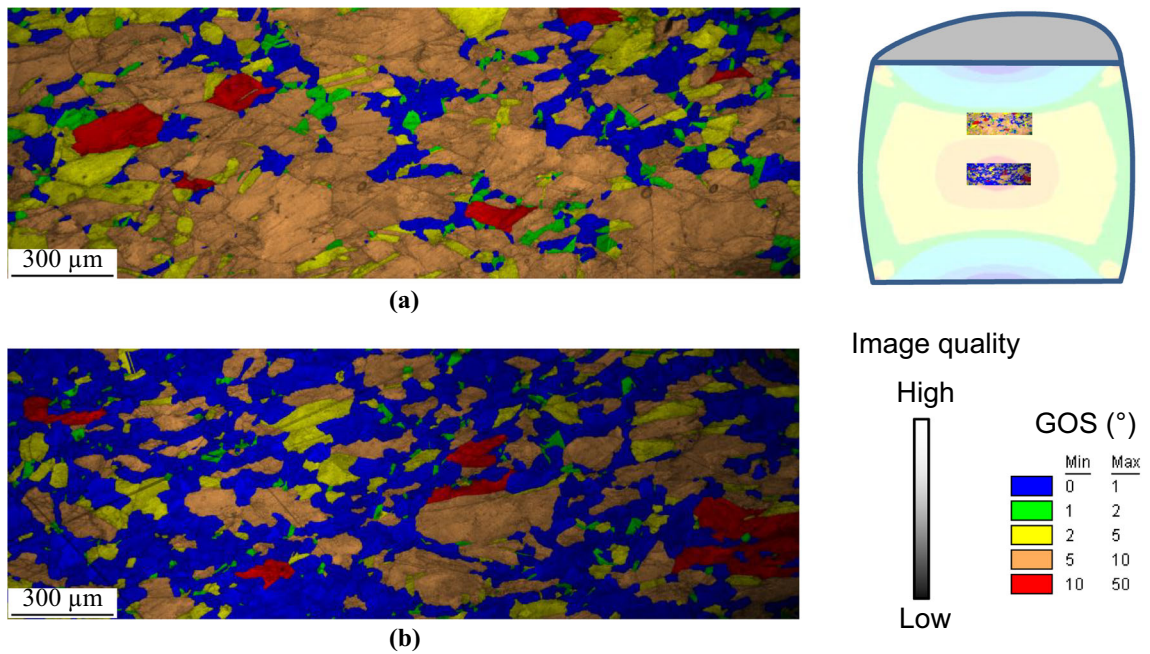


Fig. 9—EBSD maps of a uniaxial compression specimen (GOS and image quality), 1200 °C/1 hour deformed at 1150 °C up to $\varepsilon = 0.4$, then slowly cooled. (*a*) Observation at mid-distance; (*b*) observation at the center. The location of the maps is recalled in the top right scheme. The compression axis is vertical.
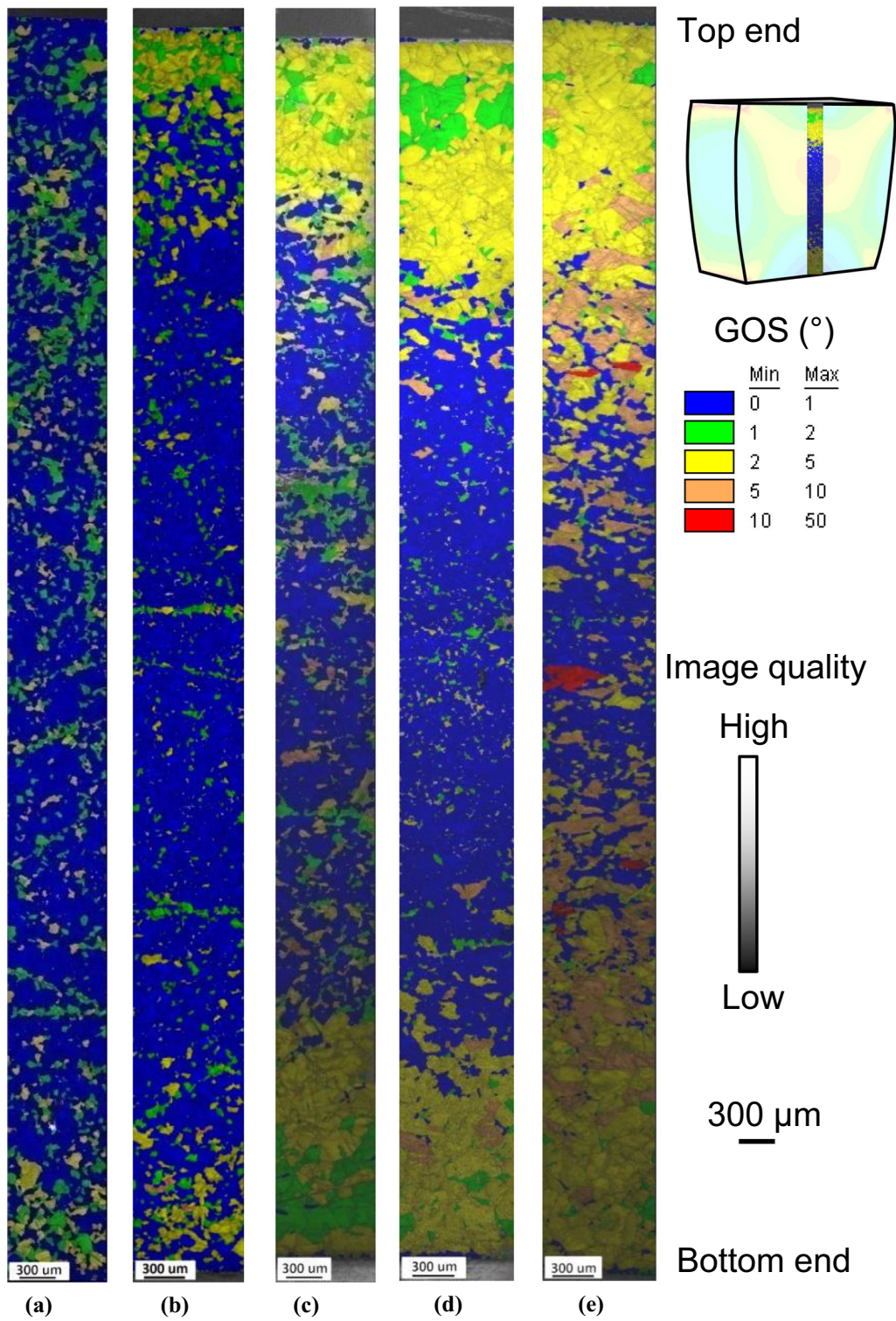
Fig. 10—EBSD maps of plane strain compression specimens (GOS and image quality), observation across the height of the specimen, after slow cooling and final annealing. (*a*) 1100 °C/1 hour, deformed $\varepsilon = 0.2$ at 1050 °C; (*b*) 1100 °C/1 hour, deformed $\varepsilon = 0.4$ at 1050 °C; (*c*) 1200 °C/1 hour, deformed $\varepsilon = 0.2$ at 950 °C; (*d*) 1200 °C/1 hour, deformed $\varepsilon = 0.4$ at 950 °C; (*e*) 1200 °C/1 hour, deformed $\varepsilon = 0.4$ at 1050 °C. The location of the maps is recalled in the top right scheme. The compression axis is vertical.
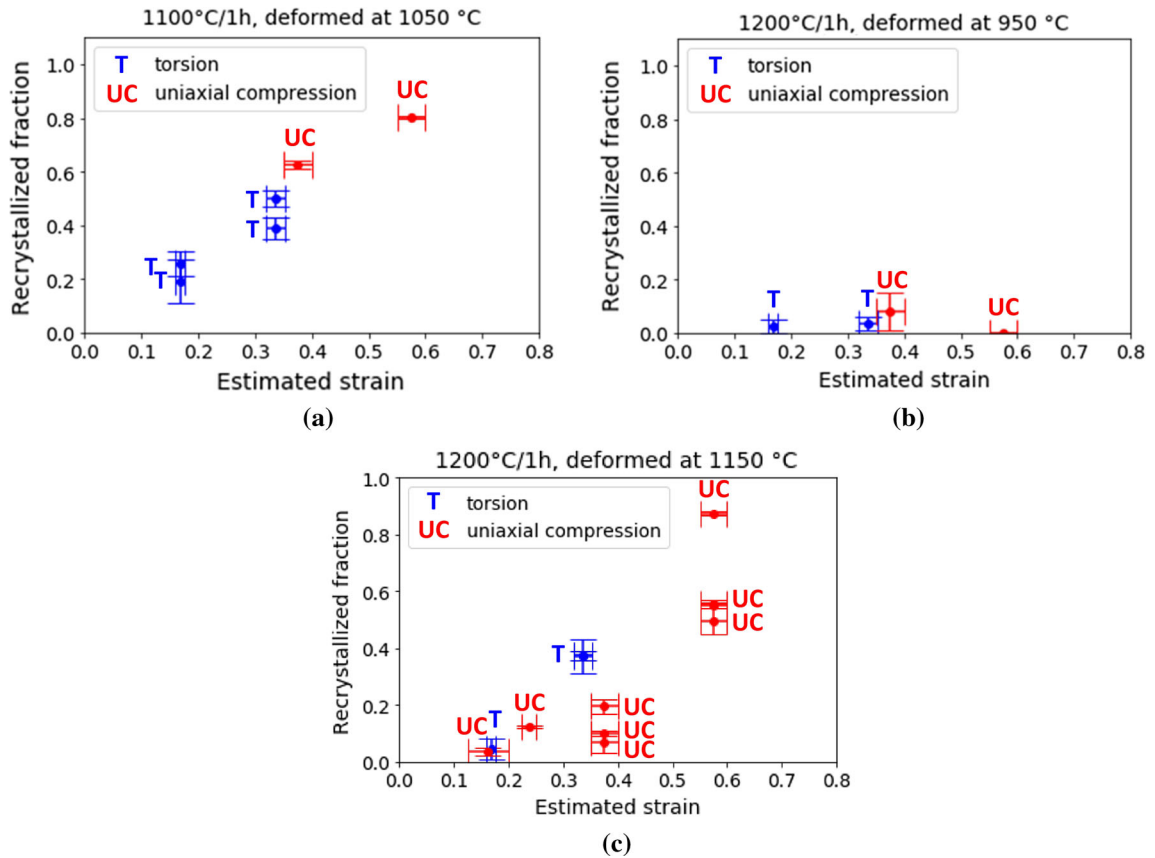
Fig. 11—Recrystallized fractions after slow cooling as a function of deformation for two different deformation modes. (*a*) Heat treated at 1100 °C then deformed at 1050 °C; (*b*, *c*) heat treated at 1200 °C and deformed at (b) 950 °C and (c) 1150 °C.

## B. *About Possible Effects of the Loading Mode on the Recrystallization Kinetics*

There are several physical reasons explaining why no measurable effect of the deformation mode was found on the recrystallization behavior of 316Nb. PDRX phenomena are known to occur in several steps:

– deformation at elevated temperature with different deformation modes,
– dynamic nucleation of (recrystallized) grains during deformation, and
– growth of the nuclei during slow cooling.

For SRX, in addition to the previous phenomena, one should also consider the following:

– static nucleation during final annealing, and
– further growth of grains originated from PDRX, and growth of static nuclei during final annealing.

Considering deformation, only relatively small amounts of strain were applied and almost no dynamic recrystallization was present here. The different deformation modes may locally create different dislocation densities, especially near grain boundaries. Yet, these differences probably remain small because of the limited macroscopic strains considered and because of the high

temperatures considered, leading to a great extent of recovery. Actually, the recovery process could vary with the deformation structure but a unique set of flow stress parameters was able to account for strain hardening in both torsion and uniaxial compression; if present, this effect is probably small. In addition, the stacking fault energy (SFE) of 316-type austenitic stainless steels is low (even if Mo or Nb can increase the SFE in our case) and this does not favor texture development especially for such small amounts of strain.

Dynamic nucleation of recrystallized grains could be dependent on the deformation path for several reasons. In 316Nb, in the investigated deformation conditions, nucleation is mainly due to serration of grain boundaries.[13] Therefore, it is mostly influenced by grain boundary mobility and by local dislocation densities close to grain boundaries. Growth of recrystallized grains at the expense of deformed ones (for both PDRX and SRX) is also mainly dictated by grain boundary mobility and by the difference in dislocation densities. Different deformation modes could induce different distributions of dislocations, especially in the vicinity of grain boundaries. However, it is again supposed that the small strains considered here are too low to lead to strong differences in dislocation structures for different loading modes. Regarding SRX, this difference is even less marked because slow cooling implied post-dynamic recovery and recrystallization. Therefore, it even more
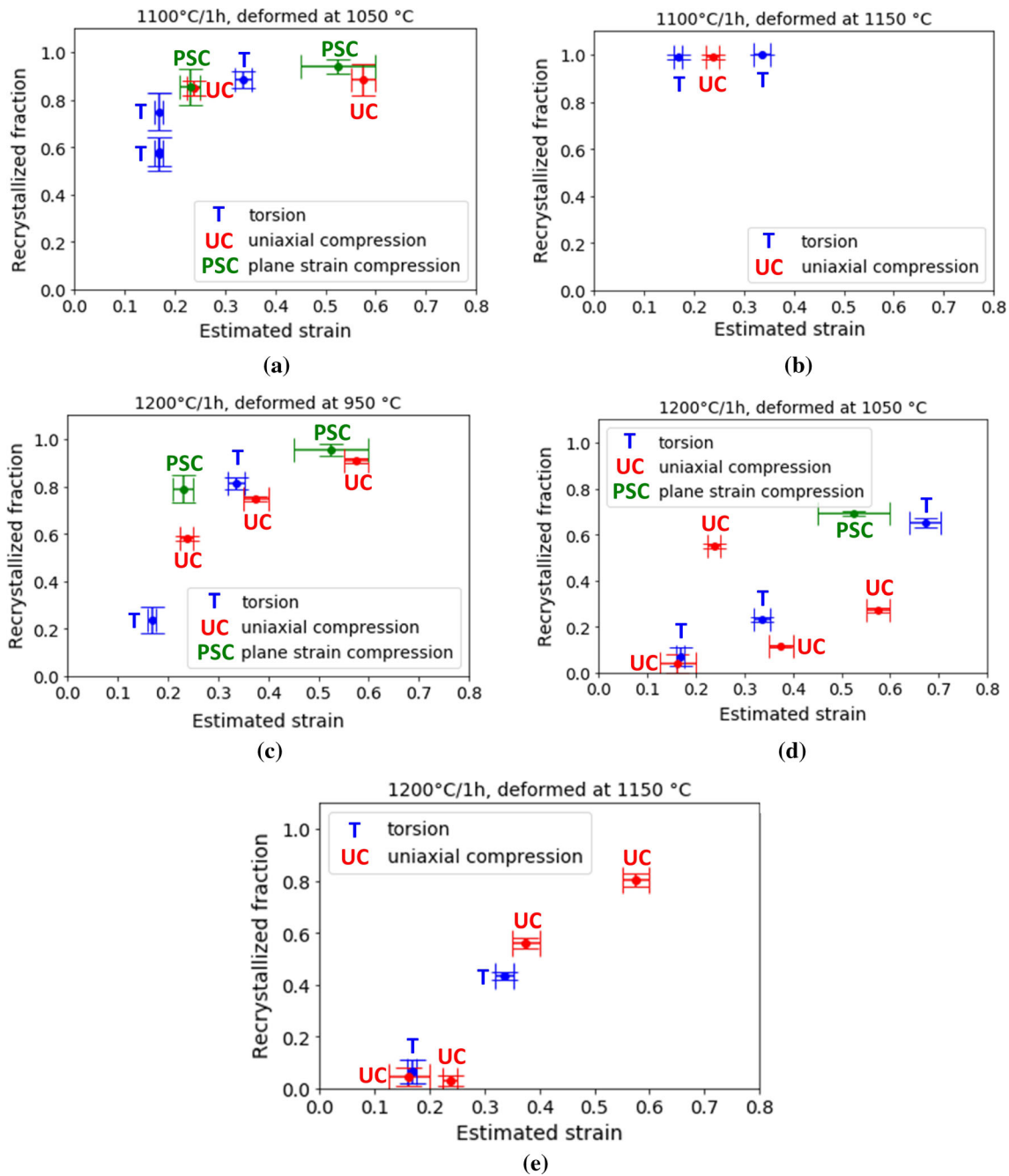
Fig. 12—Recrystallized fractions after slow cooling and final annealing as a function of deformation for three different deformation modes. (*a*, *b*) Heat treatment at 1100 °C and deformation at (a) 1050 °C and (b) 1150 °C. (*c-e*) Heat treatment at 1200 °C and deformation at (c) 950 °C, (*d*) 1050 °C, and (e) 1150 °C.

diminished the potential difference between the deformation modes. Mandal *et al.*[7] supposed that the grain boundary mobility could also be influenced by the stress state. Even if the grain boundary mobility may vary with grain boundary misorientation, this is probably not a source of major variation because the vast majority of recrystallized and deformed grains presented non-specific high-angle boundaries with almost constant mobility. A more accurate quantification of grain boundary distribution would further clarify this point.

The comparison of the SRX behaviors of 1100 °C/1 hour and 1200 °C/1 hour specimens shows that the initial heat treatment had a much stronger impact on recrystallization than the deformation mode. This effect was attributed to solute drag of niobium.[14] The effect of loading mode on solute drag-affected recrystallization is not known; from the present results, it does not strongly depend on the deformation mode. As a whole, one can conclude that no significant effect of

deformation mode on PDRX and SRX of 316Nb was evidenced in the studied conditions.

## VII. CONCLUSIONS

This study reports about any possible effect of three different deformation modes (torsion, uniaxial compression, and plane strain compression) on the flow stress and on the post-dynamic and static recrystallization behavior of 316Nb austenitic stainless steel.

A new processing method of torsion test data, based on the Hosford yield criterion and rationalized by a viscoplastic approach, was proposed. It enables to describe uniaxial compression and torsion curves in a unified manner. It still has to be generalized to other deformation modes for this material. This analysis might also readily be applied to 316L or 316L(N) steels with the same Hosford criterion. The viscoplastic self-consistent approach could be applied to determine the Hosford coefficient of any material for which a crystal plasticity model is available. In particular, this could be easily applied to other austenitic steels or to nickel-based superalloys, for which recrystallization and forging modeling is of great industrial concern.

Classical analytical solutions for plain strain compression tests were not relevant to compare flow stress curves to those of other specimens like torsion or uniaxial compression because of the many issues linked to boundary conditions.

Artifacts in the determination of local strains due to experimental testing conditions (structural effects, surface grinding of cylindrical specimens) or due to the use of the von Mises criterion can lead to wrongly conclude than a deformation mode favors recrystallization with respect to another one. Moreover, when precisely taking local strains and recrystallized fractions into account, no effect of deformation mode on the post-dynamic or the static recrystallization of 316Nb was evidenced in the studied conditions. As in torsion, the amount of Nb atoms in solid solution, linked to the initial heat treatment, might dominate the recrystallization behavior of 316Nb whatever the loading mode.

## ACKNOWLEDGMENTS

## CONFLICT OF INTEREST

The authors declare that they have no conflict of interest.

## APPENDIX A: ESTIMATION OF THE HOSFORD EXPONENT USING A SELF-CONSISTENT VISCOPLASTIC MODEL

Polycrystalline models can be used to simulate yield surfaces, and therefore, to compare flow curves using different yield criteria. In this work, we used the Berveiller–Zaoui self-consistent polycrystalline model [A1] with the Méric–Cailletaud crystal plasticity model [A2, A3]. These models are implemented in the Z-set software [A4]. No crystal plasticity parameters are available from literature for 316Nb or even for 316-type steels at elevated temperatures considered in this work. Therefore, we used the parameters given in [A5] for a 316L(N) steel at ambient temperature.

100 grains were chosen according to an isotropic orientation distribution function to represent the initial isotropic polycrystal. Pure compression and pure shear deformation at strains up to $\varepsilon = 0.05$ were considered to represent initial stages of uniaxial compression and torsion, respectively. Then, post-processing was done using Tresca, von Mises, and several values of the Hosford criterion exponent. Flow curves are given in Figure A1 for Hosford exponents $n = 8$ and $n = 20$ (Hosford 20 thereafter). One can see that for very small amounts of strain (lower than 0.005), the prediction from Hosford 8 is very close to the uniaxial compression curve but it departs for larger values of strains. On the
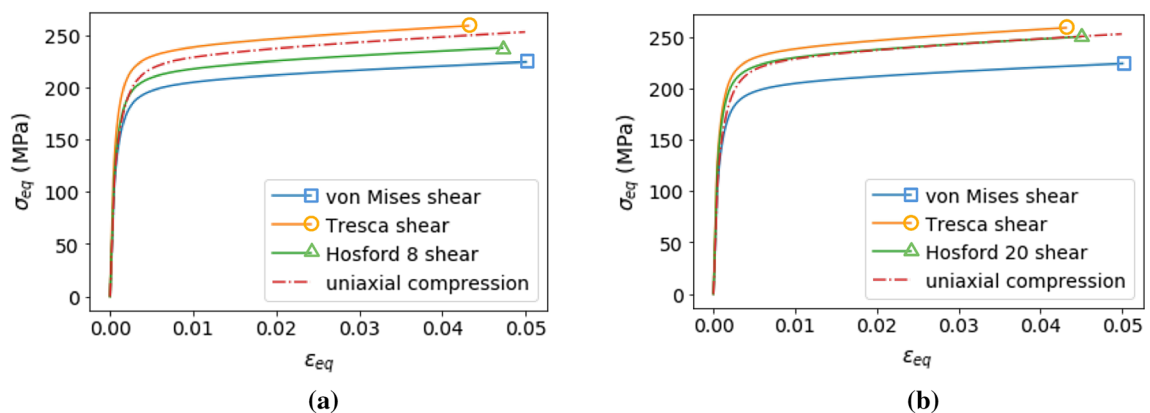


**(a)**



**(b)**

Fig. A1—Effect of the equivalent criterion chosen on the flow curves from a 100-grain simulation (*a*) Hosford exponent n = 8; (*b*) Hosford exponent n = 20. In addition to colors, one specific symbol was added at the final point of the curves for easier reference to the testing conditions, except for compression.

contrary, Hosford 20 gives slightly different predictions at very small strains but enables very good agreement between uniaxial compression and torsion curves at somewhat larger strains ($\varepsilon = 0.05$). Therefore, based on these numerical simulations, we choose the Hosford exponent $n = 20$ to describe experimental flow curves.

## REFERENCES FOR APPENDIX A

1. M. Berveiller and A. Zaoui: *J. Mech. Phys. Solids*, 1978, vol. 26, pp. 325–44. https://doi.org/10.1016/0022-5096(78)90003-0
2. L. Méric, P. Poubanne, and G. Cailletaud: *J. Eng. Mater. Technol.*, 1991, vol. 113, pp. 162–70. https://doi.org/10.1115/1.2903374
3. L. Méric, P. Poubanne, and G. Cailletaud: *J. Eng. Mater. Technol.*, 1991, vol. 113, pp. 171–82. https://doi.org/10.1115/1.2903375
4. Z-set, material and structure analysis suite. http://www.zset-software.com/, accessed on 21. May, 2021.
5. Y. Guilhem: *Numerical investigation of the local mechanical fields in 316L steel polycrystalline aggregates under fatigue loading*. PhD thesis, École Nationale Supérieure des Mines de Paris, France, 2011 (in French). https://pastel.archives-ouvertes.fr/pastel-00732147

## REFERENCES

1. L. Gavard: Dynamic recrystallization of high-purity austenitic stainless steels, PhD thesis, Grenoble INPG, France, 2001 (in French).
2. I. Weiss, T. Sakai, and J.J. Jonas: *Met. Sci.*, 1984, vol. 18, pp. 77–84. https://doi.org/10.1179/030634584790420249.
3. J.-P. Thomas: *Experimental investigation and modeling of the microstructural evolutions of superalloy 718 during hot deformation*, PhD thesis, École des Mines de Saint-Etienne, France, 2005 (in French).
4. C. Tome, G.R. Canova, U.F. Kocks, N. Christodoulou, and J.J. Jonas: *Acta Metall.*, 1984, vol. 32, pp. 1637–53, https://doi.org/10.1016/0001-6160(84)90222-0.
5. G. Zhou, Z. Li, D. Li, Y. Peng, H.S. Zurob, and P. Wu: *Int. J. Plast.*, 2017, vol. 91, pp. 48–76, https://doi.org/10.1016/j.ijplas.2017.01.001.
6. J. Humphreys, G.S. Rohrer, and A. Rollett: *Recrystallization and Related Annealing Phenomena*, 3rd ed., Elsevier, Amsterdam, 2017, pp. 13–79.
7. S. Mandal, A.K. Bhaduri, and V.S. Sarma: *Metall. Mater. Trans. A*, 2012, vol. 43A, pp. 410–14, https://doi.org/10.1007/s11661-011-1015-2.
8. C.N. Athreya, S. Suwas, and V.S. Sarma: *Mater. Sci. Eng. A*, 2019, vol. 763, p. 138153, https://doi.org/10.1016/j.msea.2019.138153.
9. E. Lindh, B. Hutchinson, and S. Ueyama: *Scr. Metall. Mater.*, 1993, vol. 29, pp. 347–52, https://doi.org/10.1016/0956-716X(93)90511-P.
10. J.D. Embury, W.J. Poole, and E. Koken: *Scr. Metall. Mater.*, 1992, vol. 27, pp. 1465–70, https://doi.org/10.1016/0956-716X(92)90129-3.
11. R.L. Barto and L.J. Ebert: *Metall. Trans.*, 1971, vol. 2, pp. 1643–49, https://doi.org/10.1007/BF02913888.
12. C.N. Athreya, A. Mukilventhan, S. Suwas, S. Vedantam, and V.S. Sarma: *Philos. Mag.*, 2017, vol. 97, pp. 3211–28, https://doi.org/10.1080/14786435.2017.1370146.
13. A. Hermant, E. Suzon, P. Petit, J. Bellus, E. Georges, F. Cortial, M. Sennour, and A.-F. Gourgues-Lorenzon: *Metall. Mater. Trans. A*, 2019, vol. 50A, pp. 1625–42, https://doi.org/10.1007/s11661-018-05103-x.
14. N. Cliche, S. Ringeval, P. Petit, J. Bellus, E. Georges, F. Cortial, J.-L. Heuzé, A.-F. Gourgues-Lorenzon, and V.A. Esin: *Metals*, 2021, vol. 11, p. 715, https://doi.org/10.3390/met11050715.
15. N. Vanderesse, C. Desrayaud, S. Girard-Insardi, and M. Darrieulat: *Mater. Sci. Eng. A*, 2008, vol. 476, pp. 322–32, https://doi.org/10.1016/j.msea.2007.04.118.
16. D.S. Fields and W. A. Backofen: *Proc. ASTM* 57, 1957, American Society for Testing Materials, West Conshohocken, PA, pp. 1259–72.
17. Z. Wenhui, S. Shuhua, Z. Deli, W. Baozhong, W. Zhenhua, and F. Wantang: *Mater. Des.*, 2011, vol. 32, pp. 4173–79, https://doi.org/10.1016/j.matdes.2011.04.043.
18. W.F. Hosford: *J. Appl. Mech.*, 1972, vol. 30, pp. 607–09, https://doi.org/10.1115/1.3422732.
19. B. Avitzur: *Metal Forming: Processes and Analysis*, Mc Graw-Hill Book Company, New York, 1968.
20. C. Chovet, C. Desrayaud, and F. Montheillet: *Int. J. Mech. Sci.*, 2002, vol. 44, pp. 343–57, https://doi.org/10.1016/S0020-7403(01)00092-3.
21. Forge® software, https://www.transvalor.com/en/blog/forge-for-open-die-forging (accessed on 24. May, 2021).
22. A. Hensel and T. Spittel: *Kraft- und Arbeitsbedarf bildsamer Formgebungsverfahren*, Leipzig Deutscher Verlag für Grundstoffindustrie, Leipzig, Germany, 1978 (in German).